

Comparison of centroid computation algorithms in a Shack–Hartmann sensor

S. Thomas,¹* T. Fusco,² A. Tokovinin,¹ M. Nicolle,² V. Michau² and G. Rousset²

¹*Cerro Tololo Inter-American Observatories, Casilla 603, La Serena, Chile*

²*ONERA, BP 72, 92322 Chatillon, France*

Accepted 2006 June 3. Received 2006 April 28; in original form 2006 February 15

ABSTRACT

Analytical theory is combined with extensive numerical simulations to compare different flavours of centroiding algorithms: thresholding, weighted centroid, correlation, quad cell (QC). For each method, optimal parameters are defined in function of photon flux, readout noise and turbulence level. We find that at very low flux the noise of QC and weighted centroid leads the best result, but the latter method can provide linear and optimal response if the weight follows spot displacements. Both methods can work with average flux as low as 10 photons per subaperture under a readout noise of three electrons. At high-flux levels, the dominant errors come from non-linearity of response, from spot truncations and distortions and from detector pixel sampling. It is shown that at high flux, centre of gravity approaches and correlation methods are equivalent (and provide better results than QC estimator) as soon as their parameters are optimized. Finally, examples of applications are given to illustrate the results obtained in the paper.

Key words: turbulence – instrumentation: adaptive optics.

1 INTRODUCTION

Adaptive optics (AO) is nowadays a mature astronomical technique. New varieties of AO, such as multi-object AO (MOAO) (Gendron et al. 2005) or extreme AO (ExAO) (Fusco et al. 2005) are being studied. These developments, in turn, put new requirements on wavefront sensing devices (WFS) in terms of their sensitivity, precision and linearity. New ideas like pyramid WFS (Ragazzoni & Farinato 1999; Esposito & Riccardi 2001) are being proposed. Yet, the classical Shack–Hartmann WFS (SHWFS), used for example in NACO the AO installed at the VLT (Rousset et al. 2003), remains a workhorse of astronomical AO systems now and in the near future.

A SHWFS samples the incident wavefront by mean of a lenslet array; the telescope aperture is divided into an array of square subapertures, which produces an array of spots on a detector. The wavefront is then analysed by measuring, in real time, the displacements of the centroids of those spots which are directly proportional to the local wavefront slopes averaged over subapertures. A good estimation of the wavefront distortion is therefore obtained from a good measurement of the spot positions. The accuracy of such measurements depends on the strength of the different noise source as well as on a non-negligible number of WFS parameters such as the detector size, the sampling factor, field-of-view (FOV) size, etc.

The goal of this study is to compare quantitatively different estimators of spot positions and suggest best suitable methods in cases

of low and high photon fluxes. In this paper, three main classes of algorithms are considered: quad cell (QC) estimator, centre of gravity (CoG) approaches and correlation (Corr) methods.

Centroid measurements are usually corrupted by the coarse sampling of the CCD, photon noise from the guide star, readout noise (RON) of the CCD, and speckle noise introduced by the atmosphere. In case of strong RON and weak signal, the spot can be completely lost in the detector noise, at least occasionally. This presents a problem to common centroid algorithms like thresholding that rely on the brightest pixel(s) to determine approximate centre of the spot. When the spot is not *detected*, the centroid calculation with such methods is completely wrong. Thus, the lowest useful signal is determined by spot detection rather than by centroiding noise.

Concerning the CoG approaches, different types of algorithms have been developed to improve the basic centroid calculation in a SHWFS: mean-square-error estimator (van Dam & Lane 2000), maximum a posteriori estimator (Sallberg, Welsh & Roggemann 1997) or Gram–Charlier matched filter (Ruggiu, Solomon & Loos 1998). Arines & Ares (2002) analysed the thresholding method. On the other hand, many parameters are involved in the estimation of the centroid calculation error as explained below, and therefore there are many ways to approach this problem. For example, Irwan & Lane (1999) just considered the size of the CCD and the related truncation problem. They concentrated on photon noise only using different models of spot shape (Gaussian or diffraction-limited spot), neglecting RON or other parameters. In this paper, we choose to focus on various causes of errors such as detector, photon noises or turbulence as well as WFS parameters. Most previous studies

*E-mail: sthomas@ctio.noao.edu

remained theoretical or compared performance to simple centroiding. Despite a large number of papers on this subject, the ultimate performance of SHWFS and a recipe of the best slope estimation method (at least in the framework of an AO loop) are still debated. Moreover, there are no clear results concerning detection limits and linearity.

As for the linearity, it is often assumed that an AO system working in a closed loop scheme keeps the spots well centred, hence linearity is not essential. However, in any real AO instrument the spots can be offset intentionally to compensate for the non-common-path aberrations (Blanc et al. 2003; Hartung et al. 2003; Sauvage et al. 2005). In critical applications such as planet detection by means of ExAO with coronagraph, a linearity of the response becomes important. It is interesting to add that it will also drive the selection of the sensing technique towards a SHWFS, as opposed to curvature sensing or pyramid (Fusco et al. 2004). The same is true for MOAO, where turbulence will be compensated in open loop relying on a SHWFS with a perfectly linear response. Our study is thus of relevance to these new developments.

Finally, an AO system working with *faint* natural guide stars (for low or medium correction level) requires a WFS with highest possible sensitivity, whereas linearity becomes less critical. Here, simple QC centroiding is often used (e.g. Herriot, Morris & Anthon 2000), despite its non-linearity. Are there any better options? As shown below, the weighted centroiding method (Nicolle et al. 2004) offers comparable noise performance while being linear.

Correlation approaches are another way to measure a spot position. Such approaches are particularly well adapted when complex and extended objects are considered (cf. Michau, Rousset & Fontanella 1992; Rimmele & Radick 1998; Poyneer, LaFortune & Awwal 2003). They have been widely used in solar AO for more than 10 yr. Here, we apply correlation centroiding to the case of a point source, select best variants of calculating the position of the correlation peak, and compare it to also other algorithms.

We begin by introducing relevant parameters and relations and by describing our technique of numerical simulations in Section 2. Different techniques of centroid measurements are discussed in detail in Section 3 (for the simple CoG), Section 4 (for the improved CoG algorithms) and Section 5 (for the Corr method). Finally, a comparison of the different methods for an ideal case and for more realistic systems is given in Section 6.

2 THE METHOD OF STUDY

2.1 Definitions

Throughout the paper, we consider only one spot in one subaperture of a SHWFS (Fig. 1). The spot is sampled by the detector within a FOV of the width W_p pixels. A spot intensity distribution $P(x, y)$ is first transformed into an array of pixel intensity values $I_{i,j}$ of the size $W_p \times W_p$, and then corrupted by photon and detector noise. These data are used to compute the spot centroid (\hat{x}, \hat{y}) , whereas the true centroid of $P(x, y)$ is located at (x_0, y_0) . The full width at half-maximum (FWHM) of the spot is N_T pixels.

Let d be the size of a square subaperture and λ the sensing wavelength. The parameter $N_{\text{samp}} = (\lambda/d)/p$ conveniently relates the angular pixel size p to the half-width of the diffraction-limited spot, λ/d . The condition $N_{\text{samp}} = 2$ corresponds to the Nyquist sampling of the spots and is used throughout this paper, unless stated otherwise. It means that for diffraction-limited spots $N_T = N_{\text{samp}} = 2$. Such sampling is close to optimum at medium or high flux (Winick 1986). When spot images

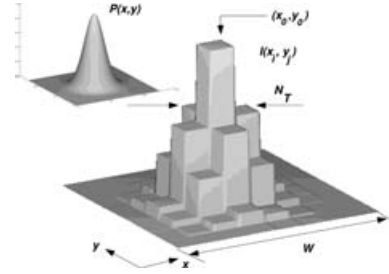


Figure 1. Some notations used in the paper. Intensity distribution in the spot $P(x, y)$ is transformed by the detector into a discrete array of pixel values $I_{i,j}$.

are very noisy, the optimum sampling corresponds to a spot FWHM of 1–2 pixels. Selecting an even coarser sampling, $N_{\text{samp}} < 1$, only increases the error. Oversampling ($N_{\text{samp}} > 2$) does not bring any additional information but increases the effect of detector noise and thus the final centroid error.

In the following, W_p is used for the FOV of the subaperture expressed in pixels and W for the same FOV expressed in λ/d .

2.2 Spot profile

Two spot models were used. The first is a two-dimensional Gaussian function:

$$P(x, y) = \frac{N_{\text{ph}}}{2\pi\sigma_{\text{spot}}^2} \exp \left[-\frac{(x - x_0)^2 + (y - y_0)^2}{2\sigma_{\text{spot}}^2} \right], \quad (1)$$

where (x_0, y_0) is the true centroid position. We introduce a random jitter of the spot centre with rms amplitude $\sigma_t = 0.1$ pixels, with the average spot position centred in the field. The FWHM of such spot is $N_T = 2\sqrt{2 \ln 2} \sigma_{\text{spot}} \approx 2.3548 \sigma_{\text{spot}}$. Gaussian spots are convenient for analytical derivations and as a benchmark for comparison with our simulations. In the following, we assimilate N_T with λ/d for convenience, using the fact that the first rough approximation of a diffraction spot is a Gaussian.

Diffraction spots formed by a square $d \times d$ subaperture and distorted by atmospheric turbulence represent a second, more realistic model. In this case, $P(x, y)$ becomes a random function and its parameters, like N_T , can be defined only in statistical sense. Atmospheric phase distortion was generated for each realization from a Kolmogorov power spectrum with a Fried parameter r_0 (at the sensing wavelength λ). The overall tilt was subtracted, and a monochromatic spot image was calculated. The true centroids (x_0, y_0) were computed for each distorted spot. We call this *realistic spot model* throughout the paper. The strength of spot distortion depends on the ratio d/r_0 : for $d/r_0 < 1$ the spots are practically diffraction limited (hence $N_T = N_{\text{samp}}$),

$$P(x, y) = N_{\text{ph}} \text{sinc}^2 \left(\frac{x}{N_{\text{samp}}} \right) \text{sinc}^2 \left(\frac{y}{N_{\text{samp}}} \right), \quad (2)$$

where $\text{sinc}(y) = \sin(\pi y)/(\pi y)$. On the other hand, for $d/r_0 > 3$ the central maximum begins to split randomly into multiple speckles.

2.3 Measurement error

As mentioned in the introduction, light intensity in each detector pixel is first corrupted by the photon noise (following a Poisson statistics) and by the additive Gaussian RON with variance N_T^2 . Moreover, centroiding errors arise from coarse sampling of the spot by CCD pixels, from truncation of the spot wings by finite size of

the subaperture field, from the spot distortions produced by atmospheric turbulence, etc. The error variance of the estimated centroid position (\hat{x}) can be expressed as

$$\sigma_x^2 = \langle (\hat{x} - x_0)^2 \rangle, \quad (3)$$

where $\langle \cdot \rangle$ represents a statistical (ensemble) average, x_0 is the real centroid position in pixels and \hat{x} is the centroid position estimated by a given algorithm. We write the estimate in a general form as

$$\hat{x} = \alpha_r x_0 + f_{nl}(x_0) + \epsilon + \text{noise}, \quad (4)$$

where α_r is a response coefficient (it remains the same whatever the spot motion), f_{nl} describes the non-linearity of the centroid algorithm, and ϵ gathers all errors due to spot shape, including truncations by the finite FOV (we often refer to these effects as ‘turbulence’). Finally, *noise* stands for errors caused by the readout and photon noise. Including equation (4) in equation (3) leads to

$$\sigma_x^2 = \langle [(\alpha_r - 1)x_0 + f_{nl}(x_0) + \epsilon + \text{noise}]^2 \rangle. \quad (5)$$

The function $f_{nl}(x)$ can be represented as Taylor expansion around $x = x_0$. The constant and linear terms are zero by definition. Assuming that $f_{nl}(x)$ is symmetric around $x = x_0$, the quadratic term vanishes as well, and we can model the non-linearity by a cubic term with a coefficient β ,

$$f_{nl}(x_0) \approx \beta x_0^3. \quad (6)$$

We can safely assume that photon and detector noises are not correlated with the shape and position of the spot. We make further, less certain assumptions that ϵ and x_0 are uncorrelated (not strictly true for truncation error) and that the response coefficient α_r is constant (true for undistorted spots, $d/r_0 < 1$, and for Gaussian spots). To simplify further, we will assume here that the centroid calculation algorithm is always adjusted to unit response, $\alpha_r = 1$. Then equation (5) becomes

$$\sigma_x^2 = \beta^2 \langle x_0^6 \rangle + \langle \epsilon^2 \rangle + \sigma_{\text{noise}}^2. \quad (7)$$

If the residual spot motion in a SHWFS is Gaussian with zero average and variance $\sigma_t^2 = \langle x_0^2 \rangle$ pixels², then $\langle x_0^6 \rangle$ which is the sixth moment of the Gaussian function is equal to $15\sigma_t^6$. The variance σ_{noise}^2 contains two independent terms related to detector ($\sigma_{N_r}^2$) and photon ($\sigma_{N_{ph}}^2$) noises. Hence

$$\sigma_x^2 = 15\beta^2 \sigma_t^6 + \sigma_\epsilon^2 + \sigma_{N_r}^2 + \sigma_{N_{ph}}^2. \quad (8)$$

It is important to remind that σ_{noise}^2 is defined here for unit response, $\alpha_r = 1$. The relative importance of each noise source changes depending on the conditions of use of the SHWFS. The strategy was to identify major noise contributors in each case and to select most appropriate centroiding algorithms. Whenever possible, the modulation of different terms in equation (8) is provided.

For example, a well-known theoretical result is that the minimum possible centroid noise for an unbiased estimator, considering a Gaussian spot with rms size σ_{spot} pixels and pure photon noise, is equal to $\sigma_{N_{ph}} = \sigma_{\text{spot}} / \sqrt{N_{ph}}$ (Winick 1986; Irwan & Lane 1999), where N_{ph} is the average number of photons per spot and per frame. Moreover, this boundary is reached by a simple centroid (Rousset 1999), which is thus the maximum likelihood estimator in this case.

Here, we also adopt the common practice of expressing centroid errors in units of phase difference across subaperture (in radians). Thus, the relation between the rms phase error σ_ϕ and the centroid error σ_x is

$$\sigma_\phi = \frac{2\pi d p}{\lambda} \sigma_x = \frac{2\pi}{N_{\text{samp}}} \sigma_x, \quad (9)$$

where λ is the sensing wavelength, d is the subaperture size and p is the angular size of the CCD pixel. We caution the reader that σ_ϕ is computed in radians for one subaperture at the WFS wavelength. To be used in calculations of AO performance, it has to be rescaled to the imaging wavelength and to the full telescope aperture, and filtered by the AO loop rejection transfer function (Madec 1999). Thus, errors exceeding 1 rad are perfectly acceptable for IR imaging when a visible-band WFS is considered. However, when, for a Gaussian spot, we reach a condition $\sigma_x \geq \sigma_{\text{spot}}$, centroid measurements become meaningless because they fail to localize spots better than the spot size. Given that $N_{\text{samp}} = N_T = 2.355 \sigma_{\text{spot}}$, this condition corresponds to $\sigma_\phi = 2\pi/2.355 = 2.67$ rad, or a variance of 7.1 rad².

2.4 Simulations

Our main technique to study various centroid algorithms consists in numerical simulation. We generate series of 1000 independent spot realizations. The intensity distribution $P(x, y)$ (either Gaussian or realistic) is computed without noise first. The pixel signals are then replaced by the Poisson random variable, with the average of N_{ph} photons per spot on a FOV W_p pixels. A zero-mean normal noise with variance N_r^2 is added to simulate the RON.

At very low light level, each simulated spot is tested for detectability. The first possible check is to have the maximum well above the RON, $I_{\text{max}} > 2N_r$. A second one is to reject the centroids with measured $|\hat{x} - x_0| > \sigma_{\text{spot}}$ or $|\hat{y} - y_0| > \sigma_{\text{spot}}$ as spurious (outside the spot). If one of those checks is not passed, the measure is assumed to have failed and therefore rejected. The number of rejected cases gives us information on the detectability limit: when more than a certain fraction of images are rejected, we consider that the centroid measurements have failed and are not reliable for those light conditions. Otherwise, the rms centroid error σ_x is computed on the retained images.

A certain fraction of frames with undetected spots is acceptable because an AO system will then simply use centroid measurements from previous frames (this only leads to an additional delay in the closed loop scheme). We set this fraction to 50 per cent and determine for each method the minimum number of photons $N_{ph, \text{min}}$ when this limit is reached. Adopting a somewhat more strict criterion (say 10 per cent invalid frames) would increase the detection threshold. The robustness of each centroiding method is characterized here by $N_{ph, \text{min}}$.

In the following we will describe the centroid algorithms considered in this study. For each method, we give a short explanation and then we focus on their advantages and drawbacks.

3 SIMPLE CENTROID (COG)

The CoG is the simplest and most direct way to calculate the position of a symmetric spot:

$$\hat{x}_{\text{CoG}} = \frac{\sum x I_{x,y}}{\sum I_{x,y}}. \quad (10)$$

This formula is widely used in AO. However, it has some limitations when using a real spot (diffraction or seeing limited) and in presence of RON. In the following, those limitations are described.

3.1 Centroid noise

Let us first recall well-known results concerning the noise of the CoG estimator. Rousset (1999) shows that for a Gaussian spot, the

photon-noise and RON contributions to phase variance are, respectively,

$$\sigma_{\phi, N_{\text{ph}}}^2 = \frac{\pi^2}{2 \ln 2} \frac{1}{N_{\text{ph}}} \left(\frac{N_{\text{T}}}{N_{\text{samp}}} \right)^2, \quad (11)$$

$$\sigma_{\phi, N_{\text{r}}}^2 = \frac{\pi^2}{3} \frac{N_{\text{r}}^2}{N_{\text{ph}}^2} \frac{N_{\text{s}}^4}{N_{\text{samp}}^2}, \quad (12)$$

where N_{T} is the FWHM of the spot in pixels, N_{r} is the readout noise, and N_{s} the total number of pixels used in the CoG calculation. It is interesting to note here that for $N_{\text{T}} = N_{\text{samp}}$, the photon-noise contribution $\sigma_{\phi, N_{\text{ph}}}^2$ reaches its Cramér–Rao bound (CRB) (Section 6.1). At low light levels, the RON contribution is dominant. It can be decreased by using the smallest number of pixels N_{s} possible in the CoG calculation. This leads to the QC method and to other modifications of the CoG considered below.

Two main hypothesis have been used to derive equation (11). First, a Gaussian spot shape has been considered whereas diffraction spots are described by equation (2). Compared to the Gaussian function, the sinc² function decreases slower in the field. In the case of a Poisson statistics (photon noise case) and considering the diffraction spot, it can be shown that (cf. Appendix A)

$$\sigma_{\phi, N_{\text{ph}}}^2 \approx 2 \frac{W}{N_{\text{ph}}}, \quad (13)$$

where W is the subaperture FOV expressed in λ/d units ($W = W_p dp/\lambda$, with p the pixel size in radians).

In this context and in presence of photon noise only, this means that the size of the window will become important for a realistic spot, while the error variance does not depend on the size of the window for a Gaussian spot. When taking into account the diffraction, the error variance increases linearly with the FOV of one lenslet, as shown in Fig. 2. Thus, for an infinite window size we get an infinite error variance. This result can be explained by the non-integrability of the function $x^2 \text{sinc}^2(x)$.

It is therefore obvious that the noise depends on the structure of the spot. This structure changes for different configurations – Gaussian spot, diffraction spot, turbulent spot – which adds some difficulties in the determination of a general theoretical expression. On the other hand, in presence of RON, the noise does not depend on the structure of the spot, since when the FOV is increased, the error due to the RON dominates the photon error.

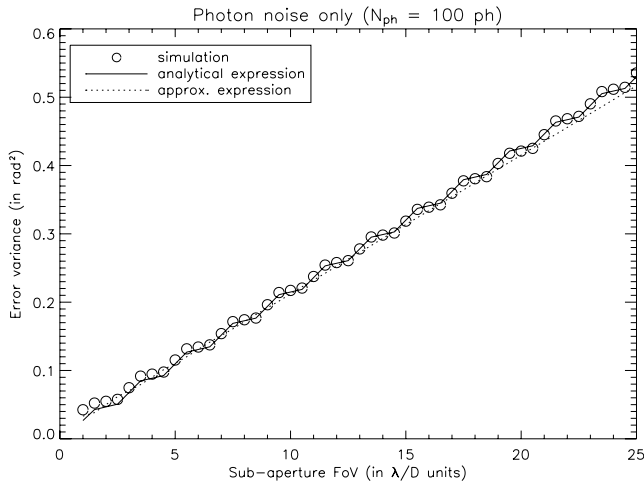


Figure 2. Error variance as a function of the FOV in presence of photon noise for a spot with a sinc² distribution.

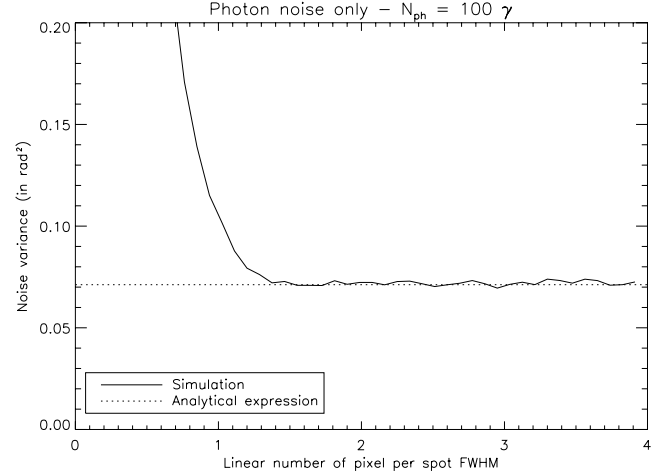


Figure 3. Validity of the analytical expression (11) for the noise influence on CoG measurements in case of Gaussian spots. Error variance as a function of the spot sampling (i.e. the number of pixels per FWHM). 2 pixels correspond to a Nyquist sampling. Photon-noise case (100 photons per subaperture and per frame).

Secondly, a Nyquist sampling criterion ($N_{\text{samp}} \geq 2$) is implicitly assumed. As shown in Fig. 3, increasing N_{samp} (typically $N_{\text{samp}} > 1.25$) does not modify the noise variance. On the other hand, taking N_{samp} smaller than 1.25 induces an additional error related to the undersampling effect. This error can be explained by non-linearity for undersampled images, as shown in the next section and in Fig. 3.

3.2 Response coefficient and non-linearity

Non-linear CoG response appears when the FOV is too small in comparison to the spot size. Indeed, it is straightforward to show that the CoG is perfectly linear for infinite FOV and adequate sampling. The smaller the FOV, the larger the deviation from linearity (Fig. 4). We can easily quantify this effect for a Gaussian spot of rms size σ_{spot} centred on $(x_0, 0)$. The CoG estimate \hat{x} calculated on the finite window of size W_p pixels is (cf. Appendix B)

$$\hat{x} = x_0 - \sigma_{\text{spot}} \sqrt{\frac{2}{\pi}} \frac{e^{\zeta} - e^{\eta}}{\Phi(\zeta) + \Phi(\eta)}, \quad (14)$$

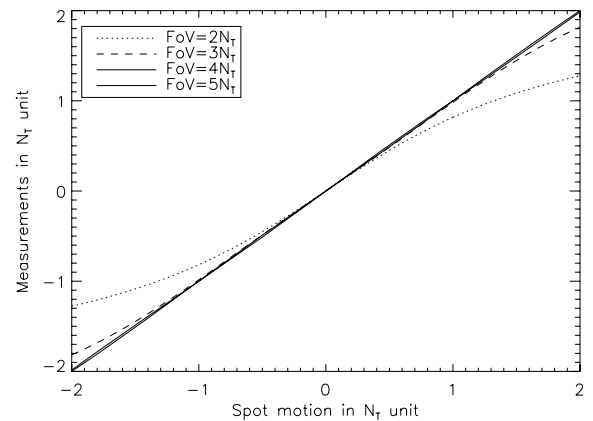


Figure 4. Linearity of the simple CoG as a function of the spot motion for different FOV sizes. The unit used here is N_{T} , FWHM of the spot.

where $\zeta = (W_p/2 - x_0)/(\sqrt{2}\sigma_{\text{spot}})$, $\eta = (W_p/2 - x_0)/(\sqrt{2}\sigma_{\text{spot}})$, and $\Phi(t) = 2/\sqrt{\pi} \int_0^t \exp(-u^2) du$.

It is interesting to note that if $W_p \rightarrow \infty$ then $\hat{x} = x_0$, in other words the CoG algorithm is asymptotically unbiased. For moderately large FOV size, $W_p/2 > 2\sqrt{2}\sigma_{\text{spot}}$, we can develop (14) in series around $x_0 = 0$, up to the third order:

$$\hat{x} \simeq x_0 - \sigma_{\text{spot}} \sqrt{\frac{2}{\pi}} e^{-(W_p/2)^2/(2\sigma_{\text{spot}}^2)} \left[\frac{W_p x_0}{\sqrt{2}\sigma_{\text{spot}}} + \frac{1}{6} \left(\frac{W_p x_0}{\sqrt{2}\sigma_{\text{spot}}} \right)^3 \right]. \quad (15)$$

We recognize here a small deviation of the response coefficient from 1 (second term) and a non-linearity proportional to x_0^3 (third term). The difference of α_t from 1 is less than 2.5 per cent for a $W = 2$ (or $W_p = 4$ for a Nyquist sampling) and <0.04 per cent for a $W = 3$ (or $W_p = 6$ for a Nyquist sampling).

Apart from the FOV size, the linearity of response is affected by sampling (Hardy 1998). This error is periodic, with the period of 1 pixel. We verified that CoG non-linearity is extremely small for reasonably well sampled spots, $N_{\text{samp}} > 1$, and becomes obvious only for very coarse sampling, $N_{\text{samp}} = 0.5$.

3.3 Atmospheric effects

The behaviour of all centroiding methods changes when we go from the Gaussian spot to a realistic diffraction spot distorted by atmospheric turbulence. In order to isolate the contribution of the atmosphere itself, we simulated recentered and noiseless spots. All methods effectively truncate outer parts of the spots and thus lead to a difference between calculated position and real CoG. This difference mainly depends on the SH FOV size W relative to λ/d and on the turbulence strength. It can be modelled as

$$\sigma_{\phi, \text{Atm}}^2 = K W^{-2} \left(\frac{d}{r_0} \right)^{5/3}. \quad (16)$$

Fits to our simulation results (Fig. 5) show that $K \simeq 0.5$ for well-sampled ($N_{\text{samp}} > 1.5$) spots (the error increases for coarser samplings). This fits has been done empirically from the simulation curves.

The origin of atmospheric centroid error can be understood as follows. The maximum intensity in the spot corresponds to a position in the FOV where the waves from subaperture interfere constructively or, in other words, to a minimum rms residual phase perturbation.

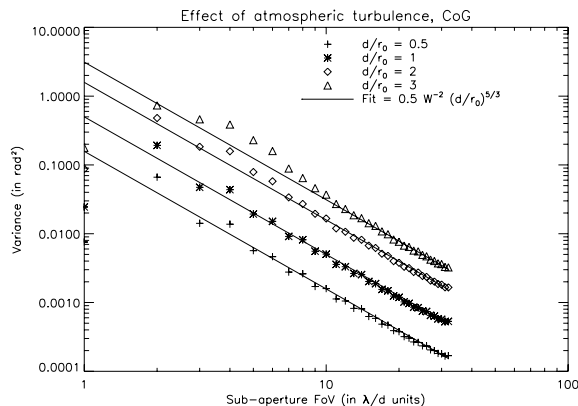


Figure 5. Illustration of the dependence of the CoG error variance on the turbulence and the subaperture FOV. The different curves represent different turbulence strengths (i.e. various d/r_0). A Nyquist-sampled spot is considered.

The best-fitting plane approximating a given wavefront corresponds to the Zernike tilt, while the true spot centroid corresponds to the average phase gradient over the subaperture, called G-tilt (Tyler 1994). Formulae for both tilts and their difference are well known in case of circular apertures and lead to the expression $\sigma_{\phi, \text{Atm}}^2 = 0.241 (d/r_0)^{5/3}$ (see equation 4.25; Sasiela 1994). Most of this difference is related to the coma aberration in the wavefront over each subaperture, never corrected by the AO. Thus, even in the worst case where only the spot maximum is measured (e.g. high threshold), the atmospheric error should not exceed $0.25 (d/r_0)^{5/3}$.

The residual fitting error in an AO system with subaperture size d is of the order $0.3 (d/r_0)^{5/3} \text{ rad}^2$ (Noll 1976). It might seem that reducing the WFS measuring error much below this quantity is useless as it will not improve the Strehl ratio. However, fitting errors contain mostly high spatial frequencies and hence scatter light into the distant wings of the compensated point spread function (PSF). The residual PSF intensity at distances from λ_i/D to λ_i/D (where D is the telescope diameter and λ_i is the imaging wavelength) is directly related to the WFS errors, dominated by $\sigma_{\phi, \text{Atm}}^2$ in case of bright stars and unfortunate choice of centroiding algorithm.

3.4 CoG: the necessary trade-offs

The trade-offs needed to optimize a simple CoG concern the FOV and the sampling factor.

In presence of photon noise only, Nyquist-sampled images are required. Then a trade-off in terms of FOV W is needed. This trade-off depends on the photon noise error, which increases with W (cf. Section 3.1), and the atmospheric error, which decreases as W^{-2} . In this case, one can define the optimal FOV size W_{opt} by minimizing the sum of equations (13) and (16).

$$\sigma_{\text{noise+atm}}^2 = 2 \frac{W}{N_{\text{ph}}} + 0.5 W^{-2} \left(\frac{d}{r_0} \right)^{5/3}. \quad (17)$$

This leads to an analytical expression for W_{opt} :

$$W_{\text{opt}} = 1.26 N_{\text{ph}}^{1/2} \left(\frac{d}{r_0} \right)^{5/9}. \quad (18)$$

Taking, for example, $d/r_0 = 2$ and $N_{\text{ph}} = 50$, we obtain the best FOV of $6.8 \lambda/d$.

This zero-read-noise case corresponds to electron multiplication CCDs or L3CCD, with half of the flux because of the multiple amplification stages. Equations (17) and (18) can be used with a factor of 2 in front.

In presence of detector noise, we want to decrease the number of pixels to minimize the noise at low flux. However, this configuration is not optimal at high flux, as explained earlier. It is therefore interesting to improve the simple CoG algorithm, adapting it to a large range of flux and RON. We present some optimization methods in the following.

4 IMPROVED CoG ALGORITHMS

Centroid errors due to detector noise can be reduced if we take into account only pixels with signal above certain threshold. The thresholding approach is detailed in Section 4.1. Recently, it has been proposed to weight pixels depending on their flux and RON. This method is called the weighted CoG (WCoG) (Nicolle et al. 2004) and is detailed in Section 4.2.

4.1 Thresholding (TCoG)

Compared to the simple CoG, the thresholding method is used to follow the spot and therefore avoids the non-linearity problems (if the threshold value is not too high). However, the truncation effects are still present since we take into account only a fraction of all pixels.

There are many ways to select pixels with high flux. We could consider a fixed number of brightest pixels or choose pixels with values above some threshold. We use the following method. The pixel with the maximum value I_{\max} is first determined, then the threshold I_T is set to $I_T = TI_{\max}$, where T is a parameter to be optimized. I_T is then subtracted from the spot image and the centroid is computed using only pixels with non-negative values, such as

$$\hat{x}_{\text{TCoG}} = \frac{\sum_{I > I_T} x(I - I_T)}{\sum_{I > I_T} (I - I_T)}. \quad (19)$$

It is important to subtract the threshold before the CoG calculation. Indeed, it can be shown that otherwise, the response coefficient α_r will be less than 1, i.e. the estimate \hat{x}_{TCoG} will be intrinsically biased.

In the low-flux regime, it may be difficult to detect spot maximum against the RON. Therefore, we add the following condition: the threshold is set to $I_T = \max(TI_{\max}, mN_r)$. The choice of m depends on a trade-off between robustness ($m > 3$ required) and sensitivity ($m \sim 1$ is better). We choose $m = 3$.

The noise of thresholded CoG can still be computed with equations (11) and (12), where N_s^2 represents the average number of pixels above threshold. By reducing N_s^2 , we diminish σ_{ϕ, N_r}^2 but increase the error due to the atmospheric turbulence. Hence, there is a compromise to find for T to optimize the threshold I_T as a function of N_{ph} .

In conclusion, thresholding resolves only part of our problems, such as the noise at medium flux. It is also very simple to implement. However, it is not optimal as it is difficult, for example, to choose pixels to be considered and their number (Arines & Ares 2002). In the next section we present a more efficient method proposed recently.

4.2 The weighted centre of gravity

The idea of the WCoG is to give weight to the different pixels depending on their flux – a kind of ‘soft’ thresholding. The contribution of the noisy pixels with very little signal – outside the core of the spot – is attenuated but not eliminated. Let us define $(F_w)_{x,y}$ the weighting function of FWHM N_w . Then the WCoG centroid is computed as

$$\hat{x}_{\text{WCoG}} = \gamma \frac{\sum x I_{x,y} (F_w)_{x,y}}{\sum I_{x,y} (F_w)_{x,y}}. \quad (20)$$

The coefficient γ is needed to ensure unit response, $\alpha_r = 1$. We can simply specify a circular window of radius r , $(F_w)_{x,y} = 1$ for $\sqrt{x^2 + y^2} < r$, or a square window. However, a better choice of the weighting function $(F_w)_{x,y}$ (i.e. different from a constant) is needed to optimize the performance of the centroid algorithm, as shown by Nicolle et al. (2004).

The WCoG method exists in two versions. The weight $(F_w)_{x,y}$ can either be fixed, or re-centred on the spot (‘following weight’), in a manner similar to thresholding. The properties of these two algorithms are different. Here, we consider only a fixed weight, centred on the most likely spot position, which can be seen as an a priori information for centroid measurement. This WCoG flavour is

well suited for closed-loop AO systems where the spots are always centred.

4.2.1 Response coefficient and non-linearity

The result of the estimation of the spot position using the WCoG with fixed window would be biased if we set $\gamma = 1$. For a Gaussian spot and Gaussian weight, the WCoG response can be calculated analytically, similarly to the CoG:

$$\hat{x}_{\text{WCoG}} = \gamma \frac{\sigma_{\text{eq}}^2}{\sigma_{\text{spot}}^2} x_0 - \gamma \sigma_{\text{eq}} \sqrt{\frac{2}{\pi}} \frac{e^\zeta - e^\eta}{\Phi(\zeta) + \Phi(\eta)}, \quad (21)$$

where if σ_w^2 is the rms size of the weighting function, σ_{eq} is defined as $\sigma_{\text{eq}}^2 = \sigma_{\text{spot}}^2 \sigma_w^2 / (\sigma_{\text{spot}}^2 + \sigma_w^2)$, and the variables ζ and η are the same as in equation (14) with σ_{spot} replaced by σ_{eq} .

In order to obtain unit response, we have to set

$$\gamma = \frac{\sigma_{\text{spot}}^2}{\sigma_{\text{eq}}^2} = \frac{N_T^2 + N_w^2}{N_w^2}. \quad (22)$$

On the other hand, this method is linear.

4.2.2 Noise of WCoG

The noise of WCoG with unit response is obtained from the study of Nicolle et al. (2004), corrected by the factor γ^2 :

$$\sigma_{N_{\text{ph}}, \text{WCoG}}^2 = \frac{\pi^2}{2 \ln 2 N_{\text{ph}}} \left(\frac{N_T}{N_{\text{samp}}} \right)^2 \frac{(N_T^2 + N_w^2)^4}{(2N_T^2 + N_w^2)^2 N_w^4}, \quad (23)$$

$$\sigma_{N_r, \text{WCoG}}^2 = \frac{\pi^3}{32 (\ln 2)^2} \left(\frac{N_r}{N_{\text{ph}}} \right)^2 \frac{(N_T^2 + N_w^2)^4}{N_{\text{samp}}^2 N_w^4}. \quad (24)$$

Equations (23) and (24) were derived by assuming a Gaussian spot, a Gaussian weight and a good sampling.

We see from those formulae that for photon noise only and $N_w = N_T$, the error variance is 1.78 times larger than for simple CoG (equation 11). This factor tends to 1 when N_w increases. Therefore there is no real interest to use this method when the spot is Gaussian and in presence of photon noise only. This ideal case is only useful as an illustration. In the following we will present the advantages of WCoG.

4.2.2.1 Sampling. The analytical formulae have been obtained for a well-sampled spot. A comparison between theory and simulation is given in Fig. 6. A good match is obtained for $N_{\text{samp}} > 2$, but for coarser samplings the errors are larger than those given by equations (23) and (24). The error due to RON, $\sigma_{N_r, \text{WCoG}}^2$, reaches a minimum for $N_{\text{samp}} = 1.5$. Our simulations show that by reducing sampling from $N_{\text{samp}} = 2$ to 1.5, the $\sigma_{N_r, \text{WCoG}}^2$ is reduced by 1.35 times, not 1.77 as predicted by equation (23).

4.2.2.2 Spot shape. The contribution of RON noise to WCoG (equation 24) does not depend on the spot shape, as for the simple CoG. However, the photon noise (equation 23) does. We observe differences between analytical formulae and simulations, both for a Gaussian and for diffraction spots, and the noise depends on the FOV size (Fig. 7).

The behaviours of WCoG and simple CoG with respect to photon noise are radically different. By weighting pixels with a Gaussian function F_w , we reduce the dependence of photon noise on the FOV

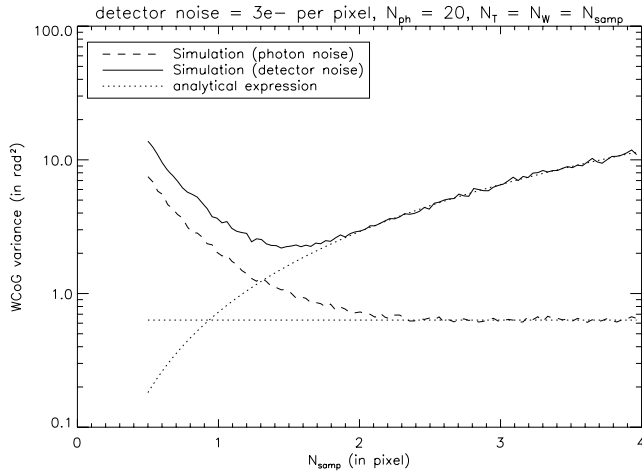


Figure 6. Error variance of WCoG as a function of the sampling, for photon noise (dashed line) and RON with $N_T = 3$ (full line). $N_{\text{ph}} = 20$ and $N_T = N_w$. The analytical expressions are plotted in dotted lines.

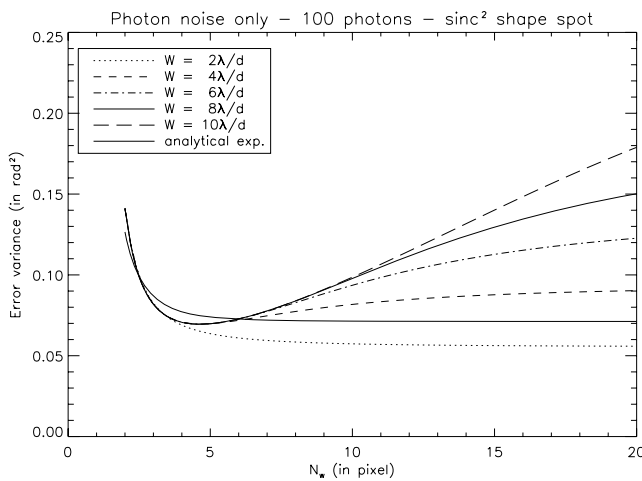


Figure 7. Influence of subaperture FOV W and of N_w on the photon noise variance with a WCoG, in presence of a diffraction spot. The number of iterations is 10000 and we took the same set of noise for each value of N_w , explaining the absence of fluctuations in the curves. The analytical curve corresponds to the equation (23) derived for a Gaussian spot.

size (as long as it is large enough, $W > 2$). There is an optimal width of the weighting function, $N_{w,\text{opt}} \simeq 4.5$ pixels (for Nyquist sampling $N_{\text{samp}} = 2$), cf. Fig. 7, that ensures the minimum photon-noise centroid variance of

$$\sigma_{N_{\text{ph}},\text{lin,opt}}^2 = \frac{7.1}{N_{\text{ph}}} \approx \left(\frac{2\pi}{N_{\text{samp}}} \right)^2 \frac{\sigma_{\text{spot}}^2}{N_{\text{ph}}}. \quad (25)$$

Therefore, by using the WCoG algorithm with diffraction spot, we can reach the same level of photon noise as for a Gaussian spot of the same FWHM. We suspect that this is close to CRB, although we did not optimize the shape of weighting function explicitly for the case of diffraction spot. The gain of WCoG over simple CoG depends on the FOV size and can be dramatic.

4.2.3 Atmospheric effects

As for the CoG, the error variance due to the atmosphere depends on the subaperture FOV, W , as shown on Fig. 8. It also depends on

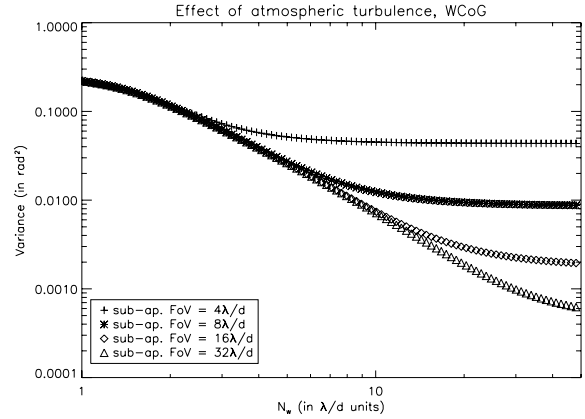


Figure 8. The variance of atmospheric error of WCoG centroids depends on the width of the weighting function N_w and on the FOV size W .

the weighting function FWHM N_w . A first approximation of this error variance is given by

$$\sigma_{\text{atmo,WCoG}}^2 \approx K (4N_w^{-2} + W^{-2}) \left(\frac{d}{r_0} \right)^{5/3}, \quad (26)$$

where N_w is in pixels and W is the FOV in λ/d units. The coefficient K is equal to 0.5 for Nyquist-sampled spot. This fit is an empirical result based on simulations.

4.2.4 Optimization

As for the CoG, there is an optimum width of the weight, N_w , depending on the noise parameters, d/r_0 , and the number of photons. For example, in the case of a detector without RON, the optimum N_w is found by minimizing the sum $\sigma_{N_{\text{ph}},\text{WCoG}}^2 + \sigma_{\text{atmo,WCoG}}^2$. Fig. 9 gives the optimum for $d/r_0 = 1$ and $N_{\text{ph}} = 100$.

4.3 Quad cell

A QC is the specific case of the CoG for a 2×2 pixels array ($N_s^2 = 4$). In this case, the FOV is given by the pixel size and by definition,

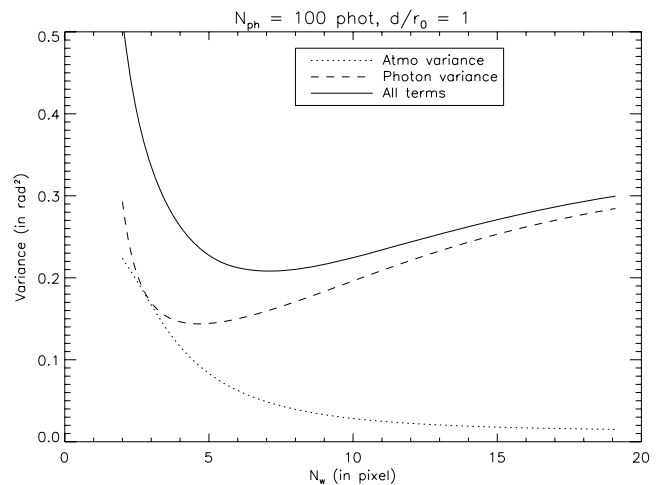


Figure 9. Trade-off for the FWHM of the weighting function. Photon-noise (dashed line) and atmospheric (dotted line) variances are plotted as a function of N_w (in pixels) for the following conditions: $d/r_0 = 1$, $N_{\text{ph}} = 100$ and $W = 8\lambda/d$. The variance sum (solid line) shows a minimum around $N_w = 7$. Nyquist-sampled spot is considered.

the spot is undersampled. QC is widely used in astronomical AO systems, e.g. in Altair (Herriot et al. 2000), because the weak signal from guide stars is better detected against RON and because, with a small number of pixels, the RON can be further reduced by a slow CCD readout. A QC algorithm calculates the centroid \hat{x}_{QC} in each direction from the differential intensity between one-half of the detector and the other,

$$\hat{x}_{\text{QC}} = \pi\gamma \frac{I_l - I_r}{I_l + I_r}, \quad (27)$$

where I_l and I_r are the intensities, respectively, on the left and the right halves of the detector and γ is the coefficient, given in pixels, translating intensity ratio into displacement, depending on the spot shape and size. For a Gaussian spot we found that $\gamma = \sigma/\sqrt{2\pi}$ pixels.

4.3.1 Noise of QC

Expression (27) leads to the following variance for photon and detector noises Rousset (1999)

$$\sigma_{\text{N}_{\text{ph}},\text{QC}}^2 = \frac{\pi^2 \kappa^2}{N_{\text{ph}}}, \quad (28)$$

$$\sigma_{\text{N}_{\text{r}},\text{QC}}^2 = 4\pi^2 \kappa^2 \left(\frac{N_{\text{r}}}{N_{\text{ph}}} \right)^2. \quad (29)$$

For a diffraction-limited spot, $\kappa = 1$. For a Gaussian spot, κ depends on the rms size of the spot. Following our definition for a Gaussian spot, the rms size is defined by σ and is given in radians in this case (and in this paper for this case only). Therefore $\kappa = \gamma 2\pi/(\lambda/d) = \sqrt{2\pi} \sigma/(\lambda/d)$. In real AO systems γ is usually variable, and considerable effort has been invested in developing methods of real-time QC calibration (Veran & Herriot 2000).

In the following, we will assume that we are able to correct for γ fluctuations, e.g. the rms size fluctuations. In our simulation, the estimation of γ has been made by first calculating the long-exposure PSF and then do linear fitting by Fourier method in order to get σ .

It is also interesting to note that nowadays, detectors in SHWFS can be photon-noise limited. In that case, the error variance ratio of the QC and the simple CoG is

$$\frac{\sigma_{\text{N}_{\text{ph}},\text{QC}}^2}{\sigma_{\text{N}_{\text{ph}},\text{CoG}}^2} = 2\ln 2 \left(\frac{\sqrt{2\pi}}{2\sqrt{2\ln 2}} \right)^2 = \frac{\pi}{2}. \quad (30)$$

The error variance of QC is 1.57 times greater than that of the simple CoG.

4.3.2 Non-linearity of QC

The response of the QC algorithm is non-linear. Elementary calculation for a Gaussian spot leads to $\beta = -1/\sigma_{\text{spot}}^2$. Hence, the non-linearity centroid error (in pixels) is $\sigma_{\text{NL}} = \sqrt{15} \sigma_{\text{spot}} (\sigma_{\text{I}}/\sigma_{\text{spot}})^3$ (cf. equation 8). It may quickly dominate other error sources even at moderate N_{ph} . On top of that, if the FOV size becomes smaller than the spot, additional non-linearity appears, similar to simple CoG.

4.3.3 Atmospheric noise

As for the previous algorithms, we study the atmospheric component of QC noise by ignoring both RON and photon-noise contributions, as well as any residual spot motion. Fig. 10 shows the error variance

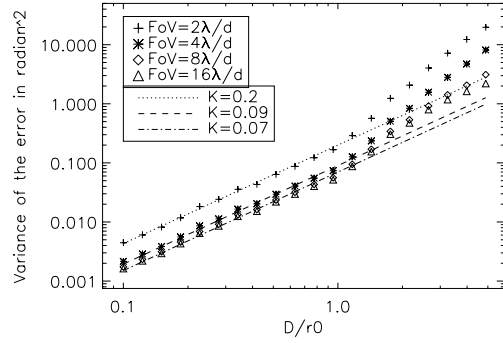


Figure 10. Atmospheric error variance of QC centroids: simulations (symbols) and models (lines).

as a function of d/r_0 for different FOV. A fit of the data leads to the following expression:

$$\sigma_{\phi,\text{Atm}}^2 \approx K_W \left(\frac{d}{r_0} \right)^{5/3}, \quad (31)$$

with K_W depending on the FOV. When the FOV is very small, the error is higher ($K_W = 0.2$) because the spot is truncated. At larger FOV, the error variance saturates at $K_W = 0.07$. This model, however, works only for low turbulence, $d/r_0 < 1$. As we see in Fig. 10, the dependence on d/r_0 becomes steeper than 5/3 power under strong turbulence. One explanation comes from the noise of γ fluctuations when $d/r_0 > 1$.

The atmospheric error barely depends on the FOV size (as soon as it is larger than a few λ/d). Even in the low-turbulence case ($K_W = 0.07$), it is 1.4 W^2 times larger than for simple CoG (cf. equation 16). In conclusion, using QC centroiding is only efficient for a noisy detector under low-flux conditions and considering small d/r_0 values. For accurate wavefront measurement and photon-noise-limited detectors other CoG methods are better.

5 CORRELATION ALGORITHM

The use of the correlation in imagery is not new and has been already proposed for AO systems that use extended reference objects, e.g. in solar observations (Michau et al. 1992; Rimmele & Radick 1998; Keller, Plymate & Ammons 2003; Poyneer et al. 2003). In this study, we apply *correlation algorithm* (COR) to a point source. First, we compute the cross-correlation function (CCF) C between the spot image I and some template F_w .

$$C(x, y) = I \otimes F_w = \sum_{i,j} I_{i,j} F_w(x_i + x, y_j + y) \quad (32)$$

and then determine the spot centre from the maximum of $C(x, y)$. The methods of finding this position are discussed below. Since the COR method is not based on the centroid calculation, it appears to be very good at suppressing the noise from pixels outside the spot. Moreover, correlation is known to be the best method of signal detection ('matched filtering'). We note that the coordinates x, y are continuous, unlike discrete image pixels, hence $C(x, y)$ can be computed with arbitrarily high resolution.

A correlation template $F_w(x, y)$ can be either a mean spot image, some analytical function or the image in one subaperture, like in solar AO systems (Keller et al. 2003).

In practice, the CCF has been calculated using Fourier transform (FT). In that case, the image has to be put in a support at least twice as big as the image size to avoid aliasing effects. The sampling of

the computed CCF can be made arbitrarily fine. One way to do this is to plunge the FT product into a grid K_e times larger, where K_e is the oversampling factor.

The behaviour of correlation centroiding with respect to the image sampling is not different from other centroid methods. At low flux – for example $N_{\text{ph}} = 30$ for $N_r = 3 e^-$ – it is slightly better to use $N_{\text{samp}} = 1.5$. However, for higher flux, undersampling ($N_{\text{samp}} < 2$) leads to a worse error variance, while for oversampling ($N_{\text{samp}} > 2$) the error variance stays the same.

We remind the reader that N_T is the FWHM of the spot image, N_w the FWHM of the template F_w . Furthermore, we will call δ the FWHM of CCF.

5.1 Determination of the CCF peak

Once the CCF is computed, it is not trivial to determine the precise position of its maximum \hat{x}_{corr} . To do this, we studied three methods: simple CoG with threshold (Noël 1997), parabola fitting and Gaussian fitting.

For the thresholding method, \hat{x}_{corr} is computed by equation (19) where I is replaced by C and I_T by $C_T = T_{\text{corr}} \max(C)$. The value of T_{corr} has been optimized in parallel with K_e . Fig. 11 shows the behaviour of the error variance for different thresholds (from $T = 0$ or $T = 0.9$).

For the parabola fitting, the determination of \hat{x}_{corr} was done separately in x and y . Three points around the maximum x_*, y_* of C along either x or y define a parabola, and its maximum leads to the \hat{x}_{corr} estimate (Poyneer et al. 2003) as

$$\hat{x}_{\text{corr}} = x_* - \frac{0.5[C(x_* + 1, y_*) - C(x_* - 1, y_*)]}{C(x_* + 1, y_*) + C(x_* - 1, y_*) - 2C(x_*, y_*)}. \quad (33)$$

In this case, a resampling of $K_e = 4$ is necessary and sufficient. For the Gaussian fitting, the one-dimensional cut through the maximum $C(x_*, y_*)$ is fitted by a Gaussian curve to find \hat{x}_{corr} .

We found that all methods of peak determination are almost identical and linear (Fig. 12) when using a Gaussian spot.

However, while the determination of the correlation peak using a few pixels around the maximum position is the best method to use in presence of RON, it is not the case in presence of atmospheric turbulence. In this latest case, information contained in the wings of the CCF is important as well. For this reason, the methods using a given function fit, such as the parabola fitting, will not be optimum.

The thresholding method on the other hand can be optimized by adapting the threshold value in function of the dominant noise. If

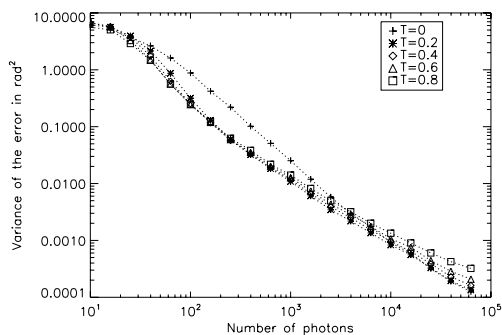


Figure 11. Error variance of \hat{x}_{corr} determined by estimation of correlation maximum using a thresholded centre of gravity with Gaussian shape spots (with FWHM = 2 pixels). The spot motion is 0.1 pixel rms. Both photon and readout ($N_r = 3$) noises are considered. Various values of threshold are used. The template image is a noise-free Gaussian $[P(x)]$.

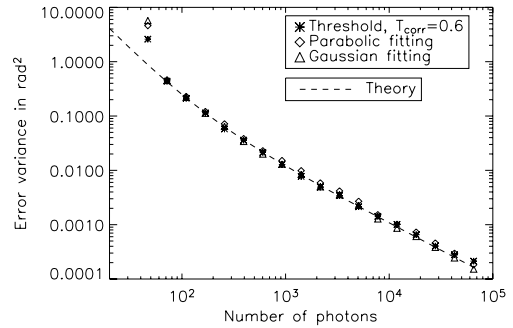


Figure 12. Comparison of three different cases of peak determination for a Gaussian spot: the thresholding, the parabola fitting and the Gaussian fitting. All methods use an oversampling factor $K_e = 8$. There is photon noise and RON ($N_r = 3$). The theory corresponds to the sum of equations (C7) and (35).

the readout noise is dominant, we will use a high value of threshold to be sensitive only to the information contained in the peak. If the atmospheric noise is dominant, we will use a very low threshold to also be sensitive to the information contained in the wings of the CCF and therefore the image itself.

Thus, for comparison with other centroid algorithms, we will use the thresholding method with a adaptable threshold.

5.2 Noise of correlation centroiding

It is possible to derive a theoretical expression of the error variance for the correlation method. The derivation in presence of RON is given in Appendix C (Michau et al. 1992).

A simplified expression of equation (C7) is

$$\sigma_{x,\text{COR},N_r}^2 = \frac{4\delta^2 N_r^2}{N_{\text{ph}}^2}, \quad (34)$$

where δ is the FWHM of $C(F_w)$, the autocorrelation function of F_w . $\sigma_{x,\text{COR},N_r}^2$ is given in pixels².

The photon noise derivation is more complex, we studied it by simulation only. Fig. 13 shows the behaviour of the correlation error variance in presence of photon noise only. A fit of the curve corresponding to the best thresholding gives

$$\sigma_{x,\text{COR},N_{\text{ph}}}^2 \approx \frac{\pi^2}{2 \ln(2) N_{\text{ph}}} \left(\frac{N_T}{N_{\text{samp}}} \right)^2. \quad (35)$$

This expression is equivalent to the error variance found in presence of photon noise only for the simple CoG. It can be shown

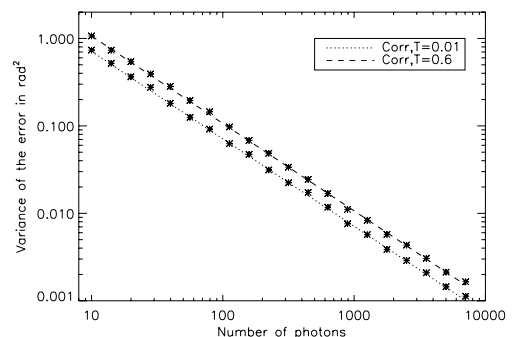


Figure 13. Error variance as a function of the number of photons for the correlation method, in presence of photon noise only, for different threshold values. The spot and template are Gaussian.

(Cabanillas 2000) that the correlation is similar to the CoG, the optimal centroid estimator (maximum likelihood) for a Gaussian spot in presence of photon noise only, if the template is the logarithm of the same Gaussian F_w . We found however that using the Gaussian distribution or the logarithm of this distribution gives very similar results.

5.3 Response coefficient and non-linearity

The response coefficient of COR used with any of the optimized peak determination methods is equal to 1. Moreover, the linearity is very good, even when using the thresholding. Indeed, $C(x, y)$ is a function which can be resampled, as explained before. This allows us to increase the value of the threshold to select only the region very close to the maximum without considering only 1 pixel.

5.4 Atmospheric noise

In this section, we study the behaviour of the correlation method in function of the size of the window used in the CCF peak determination W_{cor} and the FWHM of the template, in presence of atmospheric turbulence only. The CCF peak is determined by thresholding with $T = 0.01$, which is the best method in this particular case; it gives lower errors at high flux. It is important to also notice that using the thresholding method to determine the CCF peak allows the adaptation of the threshold value depending on the flux and readout noise. Hence, the results are more accurate than for other CCF peak determination method for any flux.

We find the same dependence of the error variance on the window size W_{cor} and the strength of the turbulence as for the simple CoG, which is

$$\sigma_{\phi, \text{cor, Atm}}^2 = K W_{\text{cor}}^{-2} \left(\frac{d}{r_0} \right)^{5/3}. \quad (36)$$

A fit to the data of Fig. 14 gives $K \simeq 0.5$ for well-sampled spots ($N_{\text{samp}} = 2$). These results are valid as long as the correlation function is not truncated (due to a high threshold for example). This K value depends obviously on the method used to determine the peak position of the correlation function. For example, the parabolic fitting is worse than the thresholding with a low threshold by a factor of 2. Indeed, the parabolic fitting take into account only the few pixels around the maximum. We saw in Section 5.1 that this was not the optimum method.

The main conclusion here is that in presence of only atmospheric turbulence, the correlation method is identical to the CoG.

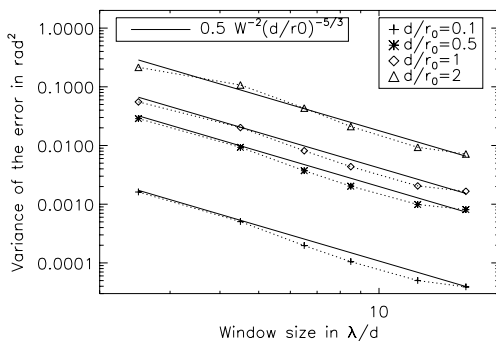


Figure 14. Error variance due to the atmospheric noise as a function of the correlation window size in λ/d for different value of d/r_0 . The model (equation 36) is overplotted as full lines. In this case $T = 0.01$.

Table 1. Computation time for different algorithms and two computers. Computer A = Intel Pentium IV 2.54 GHz, 512 Kb Cache, 1 Gb RAM. Computer B = AMD Athlon 1.1 GHz, 256 Kb Cache, 512 Kb Ram. sa = subaperture.

Computer	CoG ($\mu\text{s/sa}$)	Corr ($\mu\text{s/sa}$)
A	1	3.8
B	2.64	8.33

5.5 Computation time

We did some timing test for the CoG and the correlation for two different type of computer. The results are given in Table 1.

Those results show that the correlation is indeed slower by a factor of 3. However, depending on the requirements for the loop time, this can be acceptable. Moreover, its use in solar AO proves that the computation time is not a stopper.

6 COMPARISON BETWEEN CENTROID METHODS

6.1 The Cramér–Rao bound

The CRB is a lower boundary for the error variance of any unbiased statistical estimator. Winick (1986) applied this powerful tool to the case of SHWFS. He assumes the CCD noise to be Poisson-distributed shot noise generated by both the image spot and the detector dark current. In theory, no unbiased method can give better results than this limit. Therefore, we computed and used it in our study as a lower boundary, to compare with our simulations. Moreover, it also indicates whether the best method has been found or not.

However, it is really important to be careful with the validity of assumptions inherent to the CR method. The estimator has to be unbiased, which is the case of all the estimators considered in this study except the QC. Indeed, QC is non-linear and therefore the response coefficient α_r becomes rapidly different from 1. This explains why the QC curve goes slightly below the CR bound (e.g. Fig. 15). This is also the case for WCoG method with $\gamma = 1$.

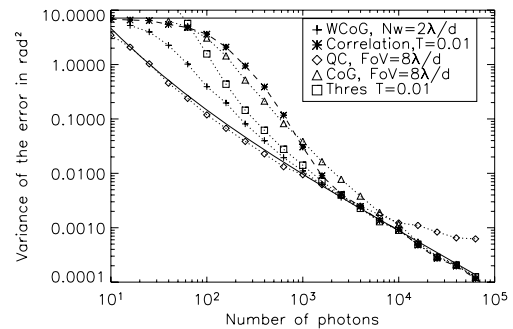


Figure 15. Comparison of different methods. Variance of the error in rad^2 in presence of photon noise and RON ($N_r = 3$). The Gaussian spot moves randomly of 0.1 pixels rms in each direction. The plain line is the CRB. The values of N_w and the FOV are given in λ/d for reference. If $T_{\text{corr}} = 0.6$ for the correlation, the error variance decreases at low flux but the noise at high flux is higher. The best way is therefore to adapt the threshold as a function of the flux and noise.

6.2 Robustness at low flux

In Fig. 15 we compare centroid methods for a Gaussian spot, at different levels of flux. The upper limit of reliable centroiding corresponds to the centroid variance equal to the rms spot size, or phase variance of 7.1 rad^2 . It turns out that the most robust method is the QC, which can give a good estimation of the spot position at 10 photons when $N_r = 3$. We recall that detection test has been implemented at low flux, explaining the behaviour (saturation) of the curves.

6.3 Comparison for a Gaussian spot

After studying in detail centroiding methods independently, the methods are intercompared. The conclusions are as follows.

(i) In presence of photon noise only, all methods after optimization are equivalent, with the exception of the QC where the error variance saturates at high flux due to the non-linearity. The motion of the spot is 0.1 pixel rms, leading to a non-linearity component equal to about $5 \cdot 10^{-4} \text{ rad}^2$.

(ii) In presence of both readout and photon noise however, the best method depends on the flux, as shown in Fig. 15. At low flux, the QC is the optimum method. Then, its error variance saturates at around $5 \cdot 10^{-4} \text{ rad}^2$ for higher flux. At higher flux, the photon noise dominates and all methods except the QC are identical. Fig. 15 shows a comparison with the CRB as well. The sampling is equal to $N_{\text{samp}} = 2$, which is the optimum for all methods at high flux. At low flux, $N_{\text{samp}} = 1.5$ gives only marginally better results, which explains why we did not consider this value.

It is possible to adapt the values of the different method's parameter as a function of flux and RON to get lower error variances. In the following, we used this adaptation in the comparison of the different methods in presence of atmospheric turbulence.

6.4 Example of results for real AO systems

Considering the high number of parameters of this study, using one method with one set of parameters only is an utopia. The solution is to adapt the parameters of each method depending on the turbulence strength, the RON and the flux.

We will give a comparison of performance for two real systems, Planet Finder (PF) (Fusco et al. 2005) and the SOAR Adaptive Module (SAM) (Tokovinin et al. 2004), working in two different configurations (Table 2). PF is a second generation extreme AO for the VLT and SAM is an AO being built for the SOAR telescope using the Ground Layer AO concept.

The first example (PF) almost can be assimilated to the case of photon noise only, which can be reached by using a new type of CCD detectors with internal multiplication, L3CCD (Basden, Haniff & Mackay 2003). As said in Section 3.4, the expected noise is then doubled since equivalent to what would be found with half the flux for conventional CCD. The second example (SAM) shows the case of common detectors where both photon and RON are

Table 2. Parameters of the study. Note that the minimum number of photons is lower for PF because of the lower detector RON value for this system.

	d/r_0	N_r	N_{ph}	N_{samp}
PF	1	0.5	$[2-10^4]$	2
SAM	2	5	$[10-10^4]$	1

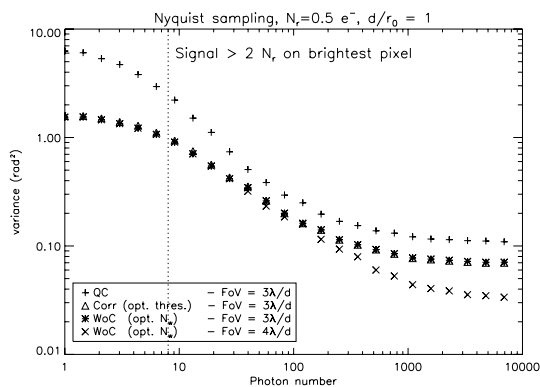


Figure 16. PF: Variance of the error in rad^2 in presence of the atmospheric turbulence ($d/r_0 = 1$) for different centroid methods. Only photon noise is considered. The vertical dotted line ($N_{\text{ph}} = 8$) represents the limit for which the signal in the brightest pixel is always greater than $2N_r$. The correlation method gives the same results as the WCoG when the same parameters are used.

present. The last difference is the sampling: Nyquist for PF and half-Nyquist for SAM. For each case, we compared the different methods described before, adapting their parameters in order to reach the best performance.

We will first comment on the detectability limit. Just as a reminder, the detectability limit is calculated from the occurrence of the maximum signal being higher than $2N_r$ over 1000 iterations (cf. Section 2.4). Here, we will show the limit for which the maximum signal is lower than $2N_r$ at least once. To give an idea for SAM, the maximum intensity of an average image is equal to about 8 per cent of the total flux when Nyquist sampled and 14 per cent when half Nyquist sampled (assuming that the centre of the spot is in between 4 pixels). We then conclude that for $N_{\text{ph},\text{min}} = 70$, the maximum intensity of the spot is too low compared to the RON, and all methods relying on this maximum (like the thresholding) are useless. This limit is equal to $N_{\text{ph},\text{min}} = 8$ for the case of PF. The values of $N_{\text{ph},\text{min}}$ decrease to a few photons for FP and to about 20 photons when we set the level of occurrence to 50 per cent.

In the following we will concentrate on the WCoG, the correlation and the QC. On the figures, we disregarded thresholding and simple CoG to avoid confusion. Those two methods are not optimal at low flux and similar to correlation and WCoG at high flux.

Case of PF. Without RON (Fig. 16), all methods are equivalent except the QC, as expected. Considering the computation time downside of the correlation, it is better to use the simple or WCoG.

The vertical dotted line ($N_{\text{ph}} = 8$) represents the limit for which the signal in the brightest pixel is always greater than $2N_r$. If the signal happens to be lower for one iteration, we remind that the measure is not taken into account (see Section 2.4).

Case of SAM. If the RON increases (Fig. 17), the results do not change when the number of photons is high enough – $N_{\text{ph}} > 300$ for $N_r = 5$ – since the error variance is limited by the atmospheric turbulence.

To reduce the impact of the noise, we used a positivity constraint (use a threshold such as $T = 0$) on the images before applying any method.

For low flux, the QC is 1.5 times better, assuming the optimistic case where the FWHM and hence the response coefficient γ are known. This is linked to the high RON and the undersampling. The two other methods however either do not rely on the knowledge of the FWHM or allow to measure the FWHM with accuracy since we

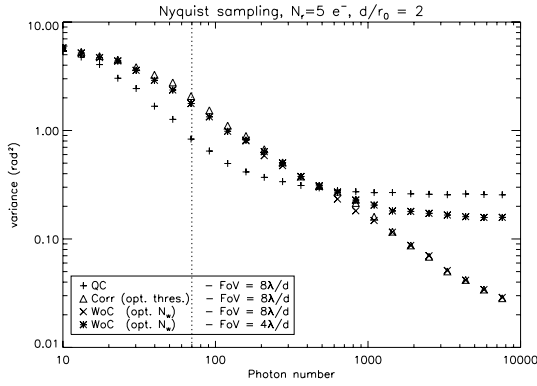


Figure 17. SAM: Variance of the error in rad^2 in presence of atmospheric turbulence ($d/r_0 = 2$) for SAM with a sampling of $N_{\text{samp}} = 1$. Both photon and RON are present. The vertical dotted line ($N_{\text{ph}} = 70$) represents the limit for which the signal in the brightest pixel is always greater than $2N_r$.

have a direct access to the shape of spot, which is not the case for QC. Moreover, the results are better at high flux. Therefore, if the error budget allows it, the simplest and more reliable method, which is the WCoG, must be chosen, even if it is not the best at low flux.

6.5 Implementation issues

From those results, it is essential to consider the implementation issues of the WFS before making a final choice. In the following, we will give some comments for the different methods.

(i) **The QC.** The advantage of this method is the low number of pixels (only 2×2), even in practice we often use more pixels. However, there is an unknown which is the exact FWHM of the spot in presence of turbulence. This FWHM must be known to get a response coefficient $\gamma = 1$. Considering the poor sampling of the image, it is difficult to calculate the spot size from the data. Moreover, this method is non-linear. The QC method can be interesting though in case of a very high RON and small values of d/r_0 .

(ii) **The CoG and its improvements.** The subaperture field is typically of 6×6 or 8×8 pixels. The pure CoG is very sensitive to noisy pixels when the signal is low compared to the RON or when the turbulence is high. Improvement can be achieved by optimizing the threshold or by using a WCoG. The last one gives the best results when adapting the rms size of the F_w as a function of flux and RON. Moreover, the response coefficient γ depends on the FWHM of the spot like for the QC. However, in that case it will be easier to determine γ since we have a direct measurement of the spot. The procedure will be to recentre and average off-line individual frames in order to obtain a recentred long exposure image and then derive the FWHM value from this direct data. Then, this value of FWHM will be used in the next measurement.

(iii) **The correlation.** The computation for this method is more complex, especially when over sampling is needed to estimate the peak position of the correlation function. The thresholded CoG gives the best estimation of the peak position of the correlation function, since the adaptation of the threshold allows to deal with either high RON or high atmospheric turbulence. Other methods are not as robust and give higher error in presence of atmospheric turbulence. The advantage of COR is that the response coefficient does not depend on the spot size and shape.

7 CONCLUSIONS AND FUTURE WORK

In this paper, we gave a practical comparison of different methods of centroid calculation in a SH wavefront sensor. We studied some variations of the centre of gravity such as WCoG, thresholding and QC. We also considered the use of the correlation to determine the spot positions. The first part of the paper was focused on the simplified case of Gaussian spot or diffraction-limited spot without atmospheric turbulence, while the second part considered all sources of error.

We are not presenting here a real recipe but a methodology to calculate the error of a SH wavefront sensor. This study can be applied to different domains by changing the parameters and the shape of the spot.

We first show a good understanding of the theory in the case of a Gaussian spot. For this particular case, the formulae can be used directly to estimate the noise in the WFS.

For diffraction-limited spot and spots distorted by atmospheric turbulence, the derivation of such formulae is more challenging. Therefore, we have studied the methods mainly by simulation. The comparison is given in two different cases: with and without RON for a strength of turbulence equal to $d/r_0 = 2$. The best method would be the WCoG, with adapting the size of the weighting function, which does not require a complicated implementation.

The correlation gives also good results and good detectability by adapting the threshold value to the flux and the RON considered. One can notice as well that at high flux, the correlation and the simple CoG give smallest errors and are similar. It is safe to say that for point sources the correlation method is not worth using, considering the complexity of its implementation. However, in presence of elongated spots it is the best method (Poyneer et al. 2003). We are planning to continue this study.

For lower turbulence, the QC is very efficient for high RON and leads to simpler detectors.

The conclusion though is that we do not have a magic method. However, the WCoG gives the optimum results independently of the signal to noise ratio when adjusting the FWHM of the weighting function. The study was made in the context of detailed designs and trade-offs where simplified analytical formula do not apply in the prediction of the WFS behaviour. We also show the complexity of the problem and the importance of the contribution of each error in the budget for the comparison of different methods (or more generally different type of WFS).

ACKNOWLEDGMENTS

This study has been financed by NOAO. We thank Lisa Poyneer and Rolando Cantarutti for useful discussions. Jean-Marc Conan and Laurent Mugnier as well were very helpful in this study.

REFERENCES

- Arines J., Ares J., 2002, *Opt. Lett.*, 27, 497
- Basden A. G., Haniff C. A., Mackay C. D., 2003, *MNRAS*, 345, 985
- Blanc A., Fusco T., Hartung M., Mugnier L. M., Rousset G., 2003, *A&A*, 399, 373
- Cabanillas S., 2000, Thesis, Aix-Marseille University
- Esposito S., Riccardi A., 2001, *A&A*, 369, L9
- Fusco T., Nicolle M., Rousset G., Michau V., Beuzit J.-L., Mouillet D., 2004, *Proc. SPIE*, 5490, 1155
- Fusco T., Rousset G., Beuzit J.-L., Mouillet D., Dohlen K., Conan R., Petit C., Montagnier G., 2005, *Proc. SPIE*, 5903, 148

- Gendron E. et al., 2005, C. R. Physique, 6, in press
- Hardy J. W., 1998, Adaptive Optics for Astronomical Telescope. Oxford Univ. Press, Oxford, p. 147
- Hartung M., Blanc A., Fusco T., Lacombe F., Mugnier L. M., Rousset G., Lenzen R., 2003, A&A, 399, 385
- Herriot G., Morris S., Anthon A., 2000, Proc. SPIE, 4007, 115
- Irwan R., Lane R. G., 1999, Appl. Opt., 38, 6737
- Keller Ch. U., Plymate C., Ammons S. M., 2003, Proc. SPIE, 4853, 351
- Madec P. Y., 1999, in Roddier F., ed., Adaptive Optics in Astronomy. Cambridge Univ. Press, Cambridge, p. 131
- Michau V., Rousset G., Fontanella J. C., 1992, in Real Time and Post Facto Solar Image Correction. Sunspot, New Mexico, p. 124
- Nicolle M., Fusco T., Rousset G., Michau V., 2004, Opt. Lett., 29, 2743
- Noël T., 1997, Thesis, ONERA, Paris
- Noll R. J., 1976, J. Opt. Soc. Am. (A), 66, 207
- Poyneer L. A., LaFortune K., Awwal A. A. S., 2003, Lawrence Livermore National Lab Report (Livermore, CA 94551)
- Ragazzoni, R., Farinato, J., 1999, A&A, 350, L23
- Rimmele T. R., Radick R. R., 1998, Proc. SPIE, 3353, 72
- Rousset G., 1999, in Roddier F., ed., Adaptive Optics in Astronomy. Cambridge Univ. Press, Cambridge, p. 115
- Rousset G. et al., 2003, Proc. SPIE, 4839, 140
- Ruggiu J.-M., Solomon C. J., Loos G., 1998, Opt. Lett., 23, 235
- Sallberg S. A., Welsh B. M., Roggemann M. C., 1997, J. Opt. Soc. Am. (A), 14, 1347
- Sandler D., 1999, in Roddier F., ed., Adaptive Optics in Astronomy. Cambridge Univ. Press, Cambridge, p. 294
- Sasiela R. J., 1994, Electromagnetic Wavepropagation in Turbulence. Springer-Verlag, Berlin
- Sauvage J.-F., Fusco T., Rousset G., Petit C., Neichel B., Blanc A., Beuzit J.-L., 2005, Proc. SPIE, 5903, 100
- Tokovinin A., Thomas S., Gregory B., van der Blik N., Schurter P., Cantarutti R., Mondaca E., 2004, Proc. SPIE, 5490, 870
- Tyler G. A., 1994, J. Opt. Soc. Am. (A), 11, 358
- van Dam M. A., Lane R. G., 2000, J. Opt. Soc. Am. (A), 17, 1319
- Véran J.-P., Herriot G., 2000, J. Opt. Soc. Am. (A), 17, 1430
- Winick K. A., 1986, J. Opt. Soc. Am. (A), 3, 1809

APPENDIX A: PHOTON NOISE EXPRESSION IN THE CASE OF A DIFFRACTION LIMITED SPOT

In the case of a diffraction limited spot and a Poisson statistics (photon noise case), the equation (11) is no longer valid. Indeed, there is some signal contained in the wings of the PSF leading to photon noise. The size of the window has to be optimized. The photon noise variance (for one direction) can be expressed for this case as

$$\sigma_{\phi, N_{\text{ph}}}^2 = \left(\frac{2\pi d}{\lambda} \right)^2 \frac{1}{N_{\text{ph}}^2} \int_{-w/2}^{w/2} \int_{-w/2}^{w/2} \alpha^2 \langle P^2(\alpha, \beta) \rangle d\alpha d\beta \quad (\text{A1})$$

with $P(\alpha, \beta)$ the sinc² shape of the spot (cf. equation 2) and w the size of the subaperture in radians. Because we are in presence of photon noise only in this case, $\langle P^2(\alpha, \beta) \rangle = P(\alpha, \beta)$ and therefore we can write

$$\sigma_{\phi, N_{\text{ph}}}^2 = \left(\frac{2\pi d}{\lambda} \right)^2 \frac{1}{N_{\text{ph}}} \int_{-w/2}^{w/2} \alpha^2 \text{sinc}^2 \left(\frac{\alpha}{\lambda/d} \right) d\alpha \int_{-w/2}^{w/2} \text{sinc}^2 \left(\frac{\beta}{\lambda/d} \right) d\beta. \quad (\text{A2})$$

We have

$$\int_{-w/2}^{w/2} \alpha^2 \text{sinc}^2 \left(\frac{\alpha}{\lambda/d} \right) d\alpha = 2 \frac{\lambda^2}{(\pi d)^2} \int_0^{w/2} \sin^2 \left(\frac{\pi d \alpha}{\lambda} \right) d\alpha = \left(\frac{\lambda}{\pi d} \right)^2 \frac{w}{2} \left[1 - \text{sinc} \left(\frac{dw}{\lambda} \right) \right], \quad (\text{A3})$$

and

$$\int_{-w/2}^{w/2} \text{sinc}^2 \left(\frac{\beta}{\lambda/d} \right) d\beta = \frac{\lambda}{\pi d} \int_0^{(\pi d/\lambda)(w/2)} \text{sinc}^2(\gamma) d\gamma, \quad (\text{A4})$$

where $\gamma = \frac{\beta}{\lambda/d}$.

Thus,

$$\sigma_{\phi, N_{\text{ph}}}^2 = \left(\frac{2\pi d}{\lambda} \right)^2 \frac{1}{N_{\text{ph}}} \left(\frac{\lambda}{\pi d} \right)^2 \frac{w}{2} \left[1 - \text{sinc} \left(\frac{dw}{\lambda} \right) \right] \frac{\lambda}{\pi d} \int_0^{(\pi d/\lambda)(w/2)} \text{sinc}^2(\gamma) d\gamma. \quad (\text{A5})$$

The function $[1 - \text{sinc}(\pi d w/\lambda)]$ tends to 1 (with some oscillations) and $\int_0^{(\pi d/\lambda)(w/2)} \text{sinc}^2(\gamma) d\gamma$ tends to $\pi/2$ when w tends to infinity (or at least if $w \gg \lambda/d$). In that case, equation (A5) can be approximated by

$$\sigma_{\phi, N_{\text{ph}}}^2 \approx \left(\frac{2\pi d}{\lambda} \right)^2 \frac{1}{N_{\text{ph}}} \frac{w}{2} \left(\frac{\lambda}{\pi d} \right)^3 \pi \approx 2 \frac{W}{N_{\text{ph}}}, \quad (\text{A6})$$

with $W = w \lambda/d$, the size of the subaperture in λ/d unit.

APPENDIX B: DERIVATION OF THE CoG ESTIMATE CALCULATED ON A FINITE WINDOW

The definition of the CoG of $P(x, y)$ on a finite window of size W_p is

$$\hat{x} = \frac{1}{P_0} \iint_{-W_p/2}^{W_p/2} x P(x, y) dx dy, \quad (\text{B1})$$

with

$$P_0 = \iint_{-W_p/2}^{W_p/2} P(x, y) dx dy \quad (\text{B2})$$

$$= \iint_{-W_p/2}^{W_p/2} \frac{N_{\text{ph}}}{2\pi\sigma_{\text{spot}}^2} e^{-[(x-x_0)^2+y^2]/2\sigma_{\text{spot}}^2} dx dy \quad (\text{B3})$$

$$= \frac{N_{\text{ph}}}{2\pi\sigma_{\text{spot}}^2} \int_{-W_p/2}^{W_p/2} e^{-(x-x_0)^2/2\sigma_{\text{spot}}^2} dx \quad (\text{B4})$$

$$\int_{-W_p/2}^{W_p/2} e^{-y^2/2\sigma_{\text{spot}}^2} dy. \quad (\text{B5})$$

We first get by deriving the expression of I_0

$$P_0 = \frac{N_{\text{ph}}}{2} [\Phi(\eta) + \Phi(\zeta)] \times \Phi \left(\frac{W_p/2}{\sigma_{\text{spot}}\sqrt{2}} \right), \quad (\text{B6})$$

where $\zeta = (W_p/2 - x_0)/(\sqrt{2}\sigma_{\text{spot}})$, $\eta = (W_p/2 + x_0)/(\sqrt{2}\sigma_{\text{spot}})$, and $\Phi(t) = 2/\sqrt{\pi} \int_0^t \exp(-u^2) du$.

Then from equation (B1), we obtain

$$\hat{x} = \frac{1}{P_0} \iint_{-W_p/2}^{W_p/2} x \frac{N_{\text{ph}}}{2\pi\sigma_{\text{spot}}^2} e^{-[(x-x_0)^2+y^2]/2\sigma_{\text{spot}}^2} dx dy \quad (\text{B7})$$

$$= \frac{1}{P_0} \int_{-W_p/2}^{W_p/2} x e^{-(x-x_0)^2/2\sigma_{\text{spot}}^2} dx \quad (\text{B8})$$

$$\int_{-W_p/2}^{W_p/2} e^{-y^2/2\sigma_{\text{spot}}^2} dy. \quad (\text{B9})$$

This leads to

$$\hat{x} = x_0 - \sigma_{\text{spot}} \sqrt{\frac{2}{\pi}} \frac{e^\zeta - e^\eta}{\Phi(\zeta) + \Phi(\eta)}. \quad (\text{B10})$$

The derivation for the WCoG is similar, taking

$$\hat{x} = \frac{1}{P_0} \iint_{-W_p/2}^{W_p/2} x P(x, y) F_w(x, y) dx dy, \quad (\text{B11})$$

where F_w is the weighting function, and

$$P_0 = \iint_{-W_p/2}^{W_p/2} P(x, y) F_w(x, y) dx dy. \quad (\text{B12})$$

APPENDIX C: RON CALCULATION FOR THE CORRELATION METHOD

Here, we consider the case where the reference F_w is a known, deterministic function. Let s be the threshold and D the domain where $C(x, y) \geq s$, and D_c the domain where the functions are defined. Then

$$x_{\text{corr}} = \frac{\int_D x [C(x, y) - s] dx dy}{\int_D [C(x, y) - s] dx dy} = \frac{N_g}{D_g}, \quad (\text{C1})$$

where N_g is the numerator and D_g the denominator. If we assume that the fluctuations of D_g are negligible compared to those of N_g , we find that

$$\sigma_{x,\text{COR}}^2 = \frac{\langle N_g^2 \rangle - \langle N_g \rangle^2}{D_g^2}, \quad (\text{C2})$$

where

$$\langle N_g^2 \rangle - N_g^2 = \int_D \int_D x x' \sigma_C^2(x, y, x', y') dx dy dx' dy', \quad (\text{C3})$$

where $\sigma_C^2(x, y, x', y')$ is the variance of the correlation function. We can show that

$$\begin{aligned} \sigma_C^2(x, y, x', y') = & \int_{D_c} \int_{D_c} F_w(u, v) F_w(u', v') [\langle I(u+x, v+y) I(u'+x', v'+y') \rangle \\ & - \langle I(u+x, v+y) \rangle \langle I(u'+x', v'+y') \rangle] du dv du' dv'. \end{aligned} \quad (\text{C4})$$

Since

$$\begin{aligned} & [\langle I(x, y) I(x', y') \rangle - \langle I(x, y) \rangle \langle I(x', y') \rangle] = \\ & \begin{cases} \sigma_b^2(x, y), & \text{if } (x, y) = (x', y') \\ 0, & \text{if } (x, y) \neq (x', y') \end{cases} \end{aligned} \quad (\text{C5})$$

where $\sigma_b(x, y)$ is the noise density. In presence of readout noise, which is a white noise, σ_b is a constant equal to N_r .

$$\sigma_C^2(x, y, x', y') = N_r^2 \int_{D_c} F_w(u, v) F_w(u+x-x', v+y-y') du dv. \quad (\text{C6})$$

Therefore, a development of equation (C2) gives

$$\sigma_{x,\text{COR},N_r}^2 = N_r^2 \frac{\int_D \int_D x x' [C_{(F_w)}(x-x', y-y')] dx dy dx' dy'}{\langle D_g \rangle^2}, \quad (\text{C7})$$

where $C_{(F_w)}$ is the autocorrelation function of F_w . $\sigma_{x,\text{COR},N_r}^2$ is given in pixels².

A simplified expression of equation (C7) can be derived using the following approximation:

$$C_{(F_w)}(x, y) \approx C_I(x, y) (D_c \otimes D_c)(x, y) \quad (\text{C8})$$

close to the maximum. Then, we can fit the function near the maximum by a parabola as

$$C_I(x, y) = N_{\text{ph}}^2 \left(1 - \frac{x^2 + y^2}{2\delta^2} \right), \quad (\text{C9})$$

where δ is the FWHM of $C_{(F_w)}$.

We finally find

$$\sigma_{x,\text{COR},N_r}^2 = \frac{4\delta^2 N_r^2}{N_{\text{ph}}^2}. \quad (\text{C10})$$

This paper has been typeset from a $\text{\TeX}/\text{\LaTeX}$ file prepared by the author.